https://dx.doi.org/10.1016/j.oceaneng.2020.107240

Micro-mechanical analysis of caisson foundation in sand using DEM

Pei WANG[1,2] and Zhen-Yu YIN[1,*]

Affiliations:

[1] Department of Civil and Environmental Engineering, The Hong Kong Polytechnic University, Hung Hom, Kowloon, Hong Kong, China

2 Southern Marine Science and Engineering Guangdong Laboratory (Guangzhou), 1119 Haibin Rd., Nansha District, Guangzhou, China

[*] Corresponding authors: Dr. Zhen-Yu YIN, Tel: +852 3400 8470; Fax: +852 2334 6389; Email: zhenyu.yin@polyu.edu.hk; zhenyu.yin@gmail.com

Abstract: Caisson foundation has been widely used for offshore structures. The micro-mechanical analysis of the behaviors of a caisson foundation during its installation, operation and failure is important but not currently available. The goal of this study is to improve the understanding of the micro-mechanisms in the installation, operation and progressive failure processes of caisson foundation and provide guidance on the design. For this, the discrete element method (DEM) is adopted to investigate the interaction of caisson foundation and sand. The DEM model is first validated by comparing the results of DEM simulations and experiments, in which similar trends are found in various load-displacement curves. With the validated model, the micro-mechanical response of soils induced by the installation process is studied firstly. Then the behavior of soils during the failure of the caisson foundation, including particle displacement, rotation, and stress distribution, are investigated for cases of different loading combinations. In addition, the fabric, including contact orientation, normal contact force, and shear contact force, and its evolution are studied by dividing the soils into four different zones based on their positions and failure mechanisms. At last, the effect of dimensionally homogenous moment to horizontal load ratio (M/(DH)) is discussed.

Keywords: Caisson foundation; failure mechanism; sand; micromechanics; microstructure; discrete element method

1. Introduction

Caisson foundation, which is upside down steel or concrete tube embedded in the seabed, has been widely used for offshore structures such as oil and gas platforms, tension leg platforms and wind turbines. Compared with gravity-based foundation or pile foundation, it is more economical in both installation process and removal process. When a caisson is lowered to the seabed, the rim of the caisson cuts into the seabed due to the gravity force of the caisson. Because the weight of the caisson is usually not large enough to push the entire caisson into the seabed, the suction force, which is induced by pumping the water out of the caisson, is applied to push it to the final position. After the installation, a caisson foundation is often subjected to a combined loading condition characterized by large overturning moment and small vertical loads.

Extensive experimental tests were conducted to study the responses of caisson foundation subjected to various loading combinations. Small-scale model test, centrifuge test and full-scale test have widely been used to study the bearing capacity, penetration velocity, seepage effect, and soil-structure interaction of caisson foundations subjected to monotonic and cyclic loadings (Barari and Ibsen 2012; Cox et al., 2014; Jia et al., 2018; Kelly et al., 2006; Kou et al., 2019; Zhu et al., 2011; Zhu et al., 2019a). These experiments have been successful in providing valuable data for the foundation design and predict the mechanical response of caisson foundations. However, they are expensive and time consuming. In addition, micro-mechanical response of caisson foundations has been unfortunately ignored in experimental tests.

Besides the experiments, analytical methods are also used to describe the behaviors of caisson foundation, such as the strain-hardening plasticity model (Cassidy et al., 2006; Villalobos et al., 2009), upper bond plasticity method (Yun and Bransby 2007),

hyperplasticity theory (Nguyen-Sy and Houlsby 2005) or macro-element method (Jin et al., 2019c; Skau et al., 2018). These methods have successfully provided the bear capacity and failure mechanism of caisson foundations, but still cannot account for the micro-mechanical response.

In recently years, numerical simulation methods, such as finite element method (FEM) and finite difference method (FDM), have been more and more widely used in the study of caisson foundations (Achmus et al., 2013; Bagheri et al., 2017; Jin et al., 2019a; Jin et al., 2019b; Mehravar et al., 2016; Mehravar et al., 2017). Some mesh-free numerical methods (Ceccato et al., 2016; He et al., 2018) have also potential in the study of these soil-structure interaction problems. The FEM, FDM or mesh-free methods, which is in the framework of continuum mechanics, has a high computational efficiency to simulate engineering scale problems, but the analyses highly depend on the phenomenological models of soils adopted, and the micro-mechanical behavior of particles cannot be investigated.

The micro-mechanical properties of particles have a strong influence on the macroscopic soil properties. During the insertion of the caisson, large compact force at the tip and interfacial shear may greatly change the initial micro-structures and properties of the soil. In addition, during the operation and failure processes of caisson foundation, the rotation of the caisson also induces anisotropy on particle fabric. All these features can be achieved if the discrete element method (DEM) is used. The advantage of DEM lies in that it can physically capture the behavior of particulate materials, and as a discontinuous analysis method it can simulate the large deformation and discontinuous process of discrete particle assembly under quasi-static and dynamic condition (see Cundall and Strack (1979), Jiang and Yin (2012, 2014), Jiang et al. (2016),Zhu et al. (2018; 2019b), Zhu and Yin (2019), and He et al.(2020)). Therefore, it can potentially overcome the shortcomings of FEM or FDM and is a powerful

numerical tool for computing the motion of a large number of particles in the large deformation analyses of caisson foundation. Moreover, for series of tests to compare each other, the DEM simulations can provide identical initial models which is very difficult to realize in experiments. However, it lacks the study of the micro-mechanical behavior of caisson foundation up to now.

Therefore, in this paper, the micro-mechanical behavior of caisson foundation during the insertion, operation and progressive failure processes is analyzed using DEM. Thanks to the advantages of DEM in modeling soils at the particle scale, the micro-mechanical response of soil particles is investigated. The DEM model is first validated by comparing the results of numerical simulations and experiments. Then the micro-mechanical analysis is focused on the effect of caisson insertion, soil behaviors during the progressive foundation failure, and the effect of M/(DH) on soil behavior.

2. DEM model and validation

2.1. DEM modeling of caisson foundation

In order for the DEM model to characterize the behaviors of caisson foundation, it was first calibrated with the experimental results of caisson foundation subjected to planar monotonic loading (Foglia et al., 2015). The caisson foundation model in their test has an outer diameter (D) of 300 mm, a lid thickness (t_1) of 11.5 mm, a skirt length (d) of 300 mm and a skirt thickness (t) of 1.5 mm (Figure 1). The caisson was pushed into a sand box with a dimension of 1600 mm × 1600 mm × 1150 mm by a vertical beam bolted on the lid. The sand used in experiments has a mean diameter d_{50} = 0.14 mm and uniformity coefficient C_u = 1.78, respectively. Three types of loads were considered in the test, i.e. vertical load (V), moment (M) and horizontal load (H). The pure central, vertical monotonic loading test was first performed to identify the vertical bearing capacity. Then based on the typical range of

moment dimensionally homogenous moment to horizontal load ratio (M/(DH)) of wind turbines, five displacement controlled tests with different M/(DH) ratios and constant vertical load were investigated, as shown in Table 1. The applied constant vertical load is 241N which includes the weight of the caisson and the measuring system.

It is important to mention that to achieve the research goal some assumptions and simplifications are made. For example, the seepage may decrease the bearing capacity of caisson foundation (Takahashi et al., 2014; Wu et al., 2020), and impose risks and threats to the near infrastructures (Lyu et al., 2019). However, the soil used in this study is dry sand which is same with the experiments, and the effect of ground water is not considered. In addition, the only shallow caisson foundation is investigated, and the failure mechanism is different from caisson foundation with high length/diameter ratio (Schneider and Senders 2010).

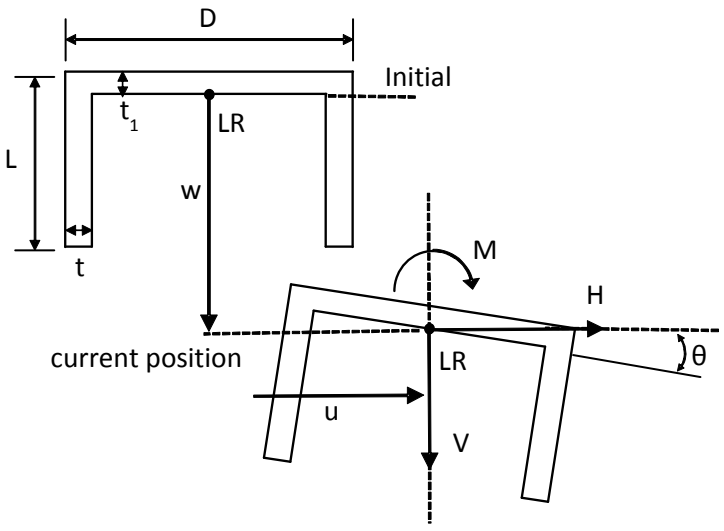

Figure 1. Sign convention for loads and displacements

Table 1 Descriptions of loading path in the test

Test name	Test details
Lab_insert	V keeps increasing until failure happens
Lab_1.1	V=241N, M/(DH) = 1.1
Lab_1.987	V=241N, M/(DH) = 1.987
Lab_3.01	V=241N, M/(DH) = 3.01
Lab_5.82	V=241N, M/(DH) = 5.82

Numerical tests in this study were performed using two-dimensional (2D) DEM code PFC2D because large number of particles raise the problem of calculation efficiency in 3D and 2D simulations have been verified and successfully applied in analyses of engineering structures in terms of trend behavior (Fu et al., 2012; Jiang and Yin 2012, 2014; Pradana et al., 2019). Load combinations in Table 1 at normal gravity condition (1g) were conducted and named as 1g_insert , 1g_1.1, 1g_1.987, 1g_3.01, 1g_5.82 and 1g_8.748. Then the gravity was increased to 10g to study the behavior of a prototype caisson foundation with a diameter of 10D (3m) subjected to same load combinations (10g_insert, 10g_1.1, 10g_1.987, 10g_3.01, 10g_5.82 and 10g_8.748). The schematic diagram of the caisson foundation DEM model is shown in Figure 2. The testing box has a rectangular shape with 1300 mm in width and 750 mm in height, and the number of soil particles in the model is around 180,000 which is determined by the size of the testing box and the relative density of the soil (0.8 in the lab tests and simulations). The particle size distribution in the DEM simulations is parallel to that of the tested sand, and the mean grain size, d_{50}, is 2.5 mm which is approximately 18 times larger than that of the tested sand to reduce the total number of particles. The caisson is modeled with a clump which is a rigid collection of disk particles rather than a wall which is a rigid surface. The advantage of using the clump method lies in its similarity with real caisson on surface roughness, geometry and self-weigh, which better reveals the micro-mechanisms during the insertion, operation and failure processes. In addition, it is also convenient to apply force and moment on a clump rather than a wall. The density of the caisson particles is set to 5605 kg/m^3 to make sure the weight of the caisson is 241 N which is same with that of the caisson in experiments. In order to obtain homogeneous specimens, the Multi-layer with Undercompaction Method (UCM) was used to generate the DEM samples (Jiang et al., 2003). The particle interactions were governed by the linear contact model in which the linear

contact force is produced by linear springs with constant normal and shear stiffness, k_n and k_s. The typical values of the stiffness k_n = 1.5×10^8 N/m and k_s = 1.0×10^8 N/m, were given. The density of sand particles is 2600 kg/m^3 and the friction coefficient is set as 0.5. The global relative density, Dr, of 80%, same with that in the experiments, is used in the DEM caisson foundation model. Figure 3 shows the typical mechanical behavior of the soils with initial relative density of 80% and 20% (before stresses applied) according to biaxial test DEM simulations at the lateral stress of 400 kPa. The soil samples are created as follows: (1) non-overlapped sand particles are randomly generated in a box, and particle properties are defined; (2) four equal-sized walls are generated outside the particle area; (3) the walls move towards soil particles so that a target confining pressure can be achieved. Then the sample is subjected to a vertical compression while the confining stress is kept constant. The shear stress is defined as $(\sigma_1 - \sigma_3)/2$ and the volumetric strain is $\varepsilon_1 + \varepsilon_3$, where σ_1, σ_3, ε_1 and ε_3 are axial stress, lateral stress, axial strain and lateral strain. The typical strain-softening and dilatancy for dense soil are successfully reproduced. For the other sample, shear stress initially increases then reaches to a peak, and the less dilatancy is observed.

The testing procedures of caisson foundation in DEM are as follows: (a) the caisson is slowly pushed into the soil at a constant velocity of 0.3 m/s until the foundation fails (in insertion test) or reaches to the final position (in constant M/(DH) tests), during which the horizontal and rotational velocity are fixed at zero; (b) the load with constant M/(DH) ratio is applied to the caisson and the corresponding displacements are monitored. And it takes about 18 hours on a workstation (Inter Xeon E5-2697A CPU and 128 GB RAM) to simulate one test. It should be noted that the goal of this paper is to investigate the mechanisms of a caisson foundation from installation to failure with different load combinations at the microscale. Therefore, the primary purpose of the 2D validation, rather than 3D, is to demonstrate that the

DEM model can reasonably capture the mechanical behaviors of caisson foundation at the laboratory scale, and lay the foundation for the following micro-mechanical analysis.

To extend the study to be more close to engineering scale, same test simulations under 1g were also repeated under 10g, as usually done by centrifuge.

Note that this work also contributes microscale characteristics references for developing the micromechanical models, such as Zhao et al. (2018a, 2018b, 2018c) and Xiong et al. (2019a, 2019b).

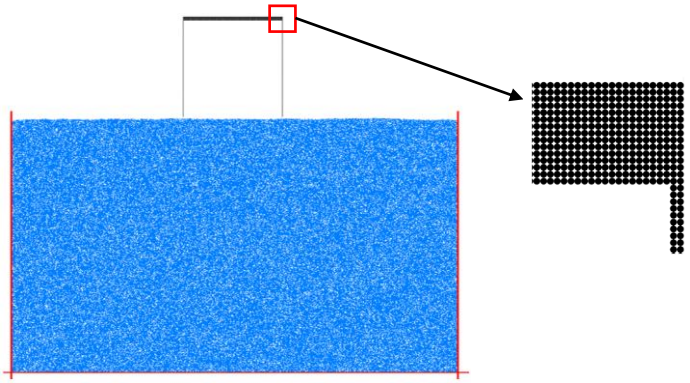

Figure 2. Schematic diagram of the caisson foundation model in DEM

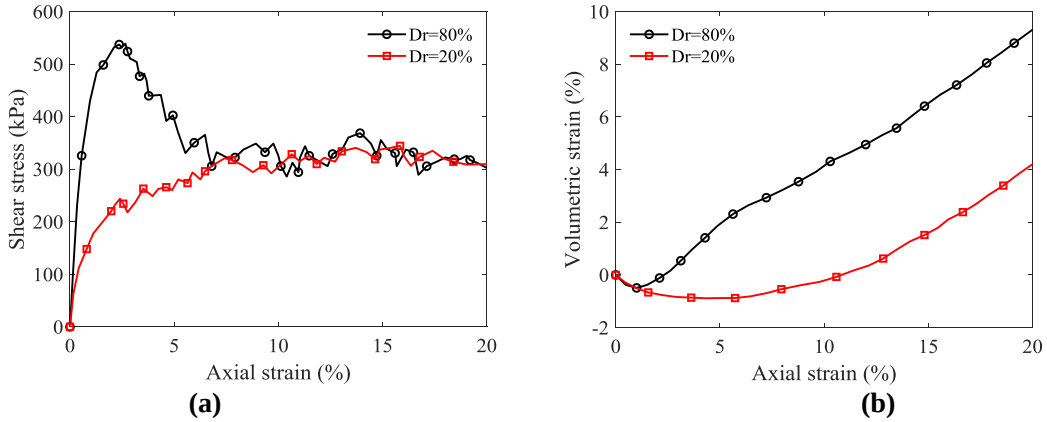

Figure 3. Results of biaxial test simulations for: (a) shear stress versus axial strain; and (b) volumetric strain versus axial strain

2.2. Results of DEM simulations

The comparison between experimental and numerical results of insertion test is shown in Figure 4. During the tests, the vertical load (V) in both experiments and numerical simulations increases with the vertical displacement, and then reaches its plateau. The value of vertical load is very low during the skirt penetration (w < 288.5 mm) and is the result of the reaction vertical force at the tip and the wall friction. Once the lid of the caisson is pushed to the seabed, the vertical load increases significantly until the foundation fails. The bearing capacity of a caisson foundation can be estimated by the point with maximum curvature, i.e. significant change in stiffness, on the load-displacement curve. Therefore, the bearing capacities of the 1g_insert and 10g_insert tests are 52 kN and 518 kN, compared with 91.66 kN in the experiment. As expected, the bearing capacity of 10g_insert test is almost ten times of that in the 1g_insert test. As is mentioned in Section 2.1, an exact match of experimental and simulated bearing capacity is of minor importance, as the goal of this validation is to demonstrate that the 2D DEM model can capture the macroscopic behavior and failure mechanism of caisson foundation. The general evolution trend of vertical force (V) is very similar in all three tests, which indicates that the 2D simulation is able to reproduce the progressive failure in the insert process.

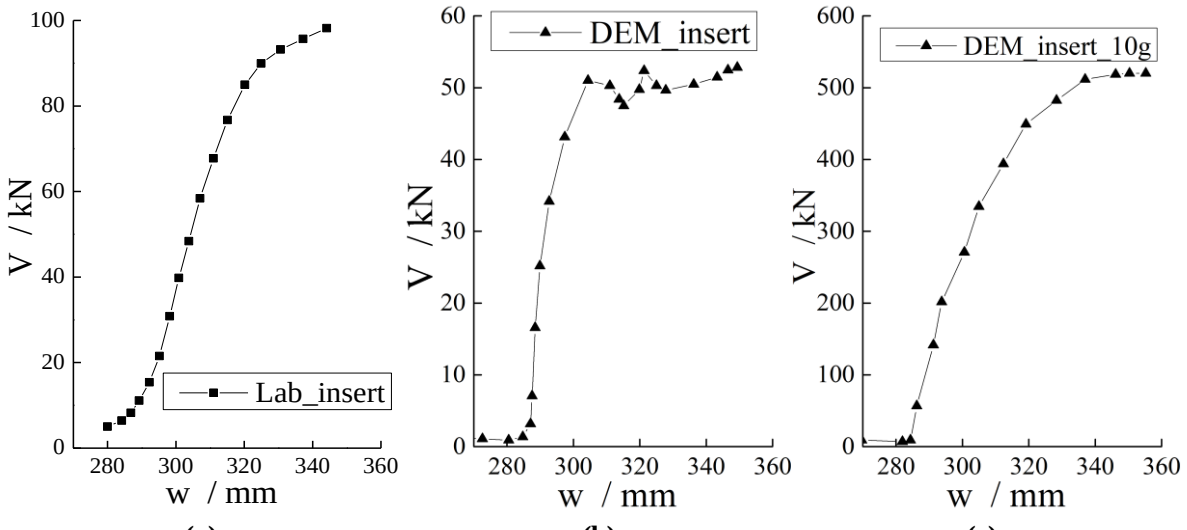

(a) **(b)** **(c)**

Figure 4. Comparison between experiments and simulation of insertion test: (a) Lab_insert; (b) 1g_insert; and (c) 10g_insert

Figure 5 shows the relationship between horizontal displacement (u) and horizontal load (H) at various M/(DH) ratios in the experiments, 1g and 10g DEM simulations. Horizontal load increases as the displacement increases with a decreasing slope and then becomes stable. For a given horizontal displacement, the test with a larger M/(DH) requires a higher horizontal force. It is also noticeable that compared with the experimental results, there are some fluctuations in the results of DEM simulations, which is common in the DEM method and could come from various factors, such as the difference in timestep, localized strong contact forces or localized particle velocity. Figure 6 shows the results of relationship between rotational displacement (Dθ) and dimensionally homogeneous moment (M/D), in which the Dθ increases with M/D and reach to a peak, similar to the trend of the u-H curves in Figure 5. Figure 7 and Figure 8 present the results of horizontal displacement (u) versus vertical displacement (w) and rotational displacement (Dθ) versus vertical displacement (w) which can both be characterized by a quasi-linear relationship. The values of displacements, including both translational and rotational, are close in experiments, 1g and 10g DEM simulations. Results also show that a foundation with a higher M/(DH) fails at much lower horizontal displacement or rotational angle. For example, the horizontal bearing capacity of the foundation in test 1g_1.1 is about four times that of the foundation in test 1g_8.748, as is shown in Figure 5. Similar result is found for the bearing capacity of moment in Figure 6. In other words, for a specific caisson foundation, the larger the overturning moment is applied to the foundation, the lower bearing capacity is obtained. To sum up, a general consistency in the evolution trend is observed between the experimental and the numerical results, which demonstrates the ability of the DEM model to simulate the behavior of caisson foundation.

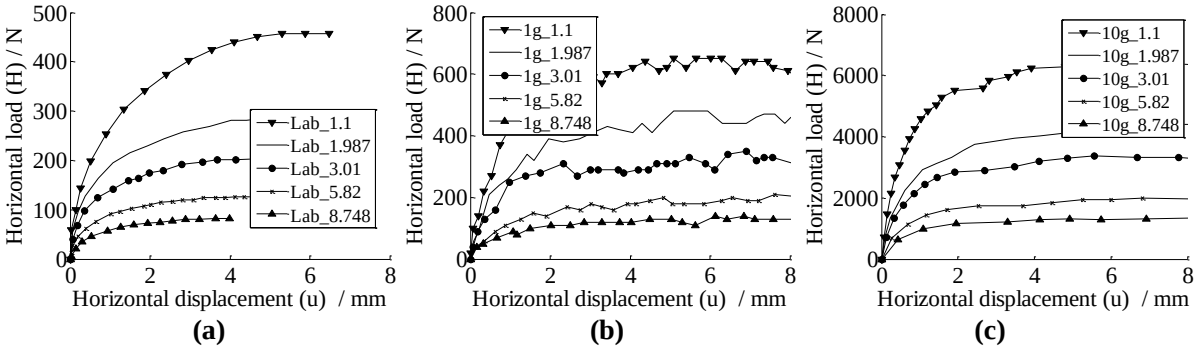

Figure 5. Horizontal displacement (u) versus horizontal load (H) in (a) experiments; (b) DEM simulations at 1g; and (c) DEM simulations at 10g

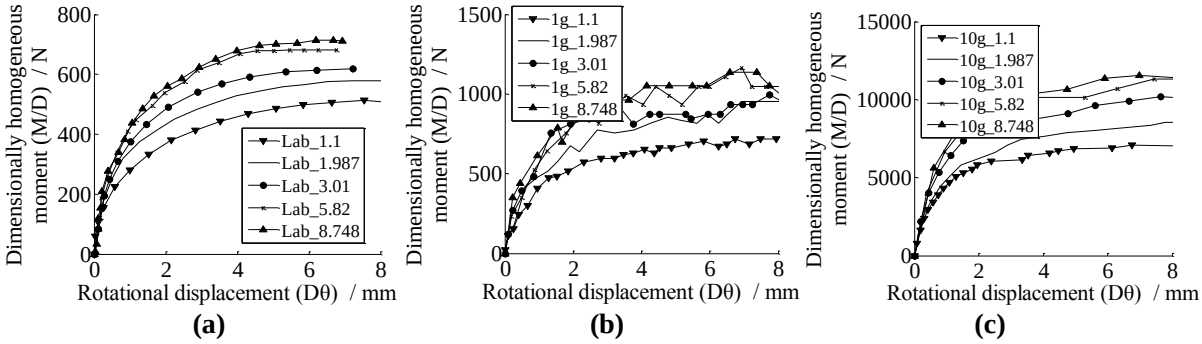

Figure 6. Rotational displacement (Dθ) versus dimensionally homogeneous moment (M/D) in (a) experiments; (b) DEM simulations at 1g; and (c) DEM simulations at 10g

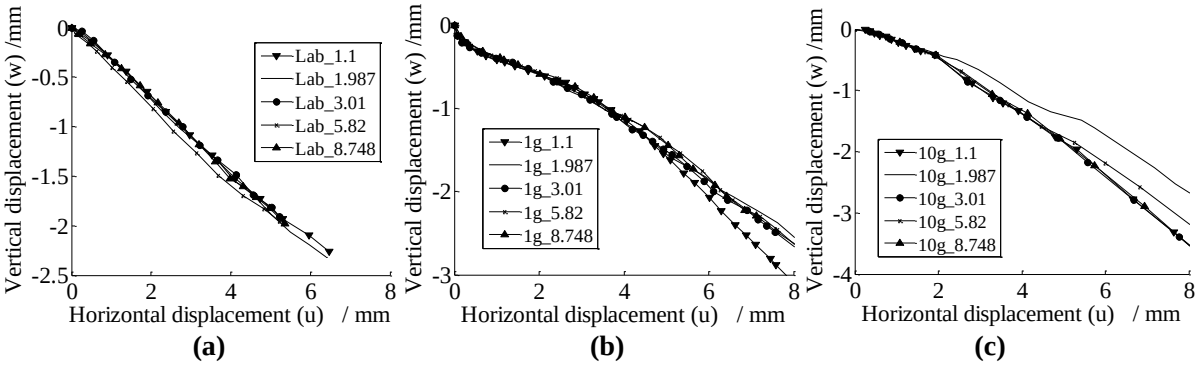

Figure 7. Horizontal displacement (u) versus vertical displacement (w)

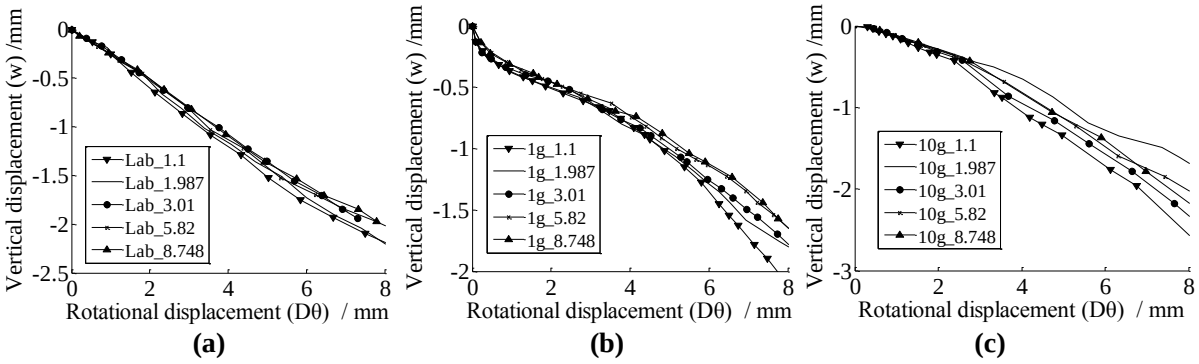

Figure 8. Rotational displacement (Dθ) versus vertical displacement (w)

3. Micro-mechanical analysis of caisson foundation

3.1. Effect of caisson insertion

The soil particle rotation and displacement after the caisson insertion are shown in Figure 9. Particles near the soil-caisson interface usually experienced large rotation due to the strong interface shear force during the insertion process, shown in Figure 9(a). According to the failure mechanism of caisson foundation proposed by (Schneider and Senders 2010), the addition of skirts moves the shallow foundation failure mechanism to deeper soil layers. Therefore, a triangular trapped soil wedge can be observed below the caisson skirt (dashed triangle in Figure 9(a)), which induces large particle rotations at the wedge boundaries. However, except for the wedge beneath the foundation, no obvious shear plane can be identified, which means the foundation failure has not been initiated. Similar observations are also reported in (Jin et al., 2019b). The wedge is found in the particle displacement field in Figure 9(b), and leads to large displacement gradients at the wedge boundaries. The vertical ground stress distribution before and after the caisson insertion is shown in Figure 10. Before the insertion process, the contour lines of vertical stress are quasi-horizontal indicating that the vertical stress increases with the depth. After the caisson is inserted, the vertical stress around the skirt is slightly increased due to the shear induced dilatancy effect and the compaction effect in which soil particles move from the tip to the skirt (Chai et al., 2014). In general, in the insertion process soils inside the caisson and the trapped triangular move downwards which generates particle rotation at the boundaries and localized stress concentration around the skirt.

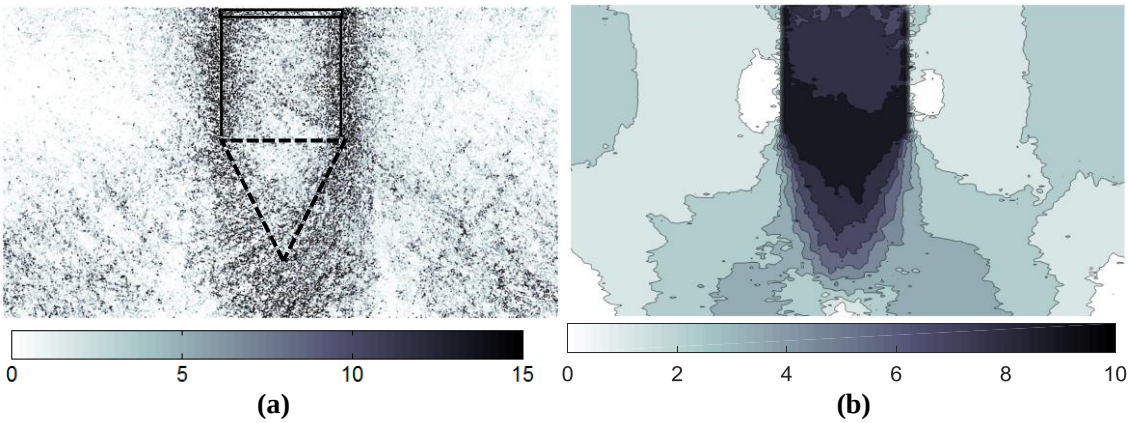

Figure 9. (a) Particle rotation and (b) particle displacement after caisson insertion

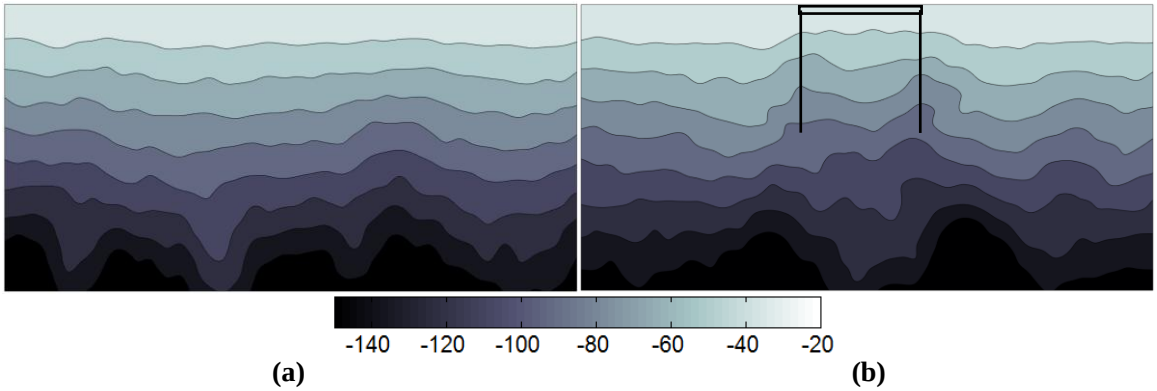

Figure 10. Vertical ground stress distribution before (a) and after (b) caisson insertion

3.2. Soil behaviors during progressive foundation failure

Because caisson foundations are often subjected to large moments, a typical failure pattern is the rotation failure. The foundation failure happens when the value of moment becomes stable and is not affected by the increase of rotational angle. According to the test results of rotational displacement (Dθ) in Figure 6, the foundation failure occurs at Dθ equal to 5.24 mm·rad which corresponds to a rotational angle of 1º. Therefore, in order to see the progressive failure of caisson foundation, the micro-mechanical analysis of caisson foundation failure is investigated at three rotational angles, i.e. 0.2°, 0.5° and 1.0°, which represents the initial stage, development stage and failure stage, respectively. Note that the following results in this section are obtained from the test 1g_1.1, and similar results from other tests are not repeated here.

3.2.1. Micro-mechanical analysis of caisson foundation failure

Figure 11 shows the particle rotation obtained from the DEM simulation 1g_1.1 when the caisson rotational angle is 0.2º, 0.5 º and 1.0º. At the initial stage (Figure 11(a)), localized particle rotation first happens outside the right skirt of the caisson. Then as the caisson continues to rotate, some particle rotations are generated outside the left skirt and beneath the caisson (Figure 11(b)). In the failure stage, large particle rotations are mainly observed near the interface between soils and the exterior face of the skirt. In addition, particle rotations outside the right skirt is larger than that on the left side due to the combination of interface shear effect and the unloading effect which results in the downward movement of the particles. What's more, particles located within the two triangular areas experienced relatively larger rotations than the rest area, and the size of the left triangle is bigger than the left one, shown in Figure 11(c). This observation during the failure of the caisson foundation here can be explained by the difference between active failure and passive failure: the active zone (right triangle) has a failure angle (57º close to $\pi/4 + \phi_p/2$, where ϕ_p is the friction angle and has the value of 26.5º) bigger than that (34º close to $\pi/4 - \phi_p/2$) of the passive case, and thus smaller area of influence.

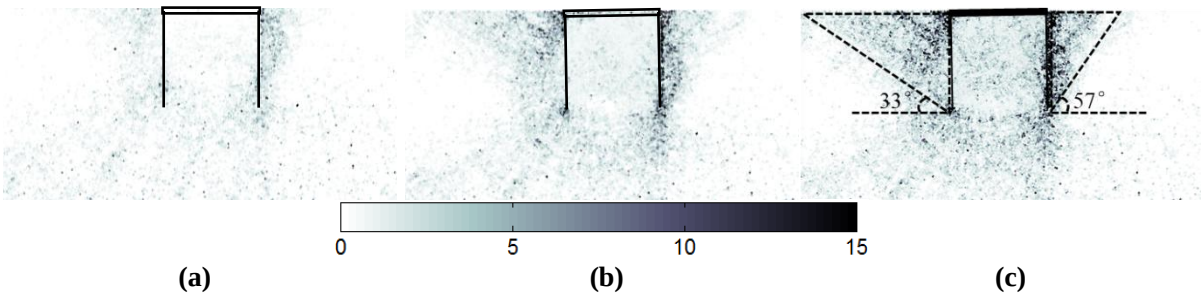

Figure 11. Particle rotation when caisson rotational angle is 0.2º (a), 0.5º (b) and 1.0º (c)

Figure 12 shows the particle displacement field when the rotation angle is 0.2º, 0.5º and 1.0 º. When the rotational angle is increased from 0.2º to 1.0º, the magnitude of particle displacement also increases significantly. Soils at the surface are subjected to larger

displacement than other areas, and the maximum displacement occurs at the upper right position of the foundation. Figure 12 also shows that the rotation center of the caisson foundation is located at the lower left part of the caisson, and has a depth of 0.8d, 0.76d and 0.78d corresponding to the rotational angle of 0.2º, 0.5º and 1.0º, where d is the length of the skirt (the embedded length of the caisson). The positons of location center in the DEM simulations are very close to 0.73d which value is proposed by Fan et al. (2006) for the rotation center of caisson foundations, and the slight difference may come from the soil grading and properties (Tang et al., 2016).

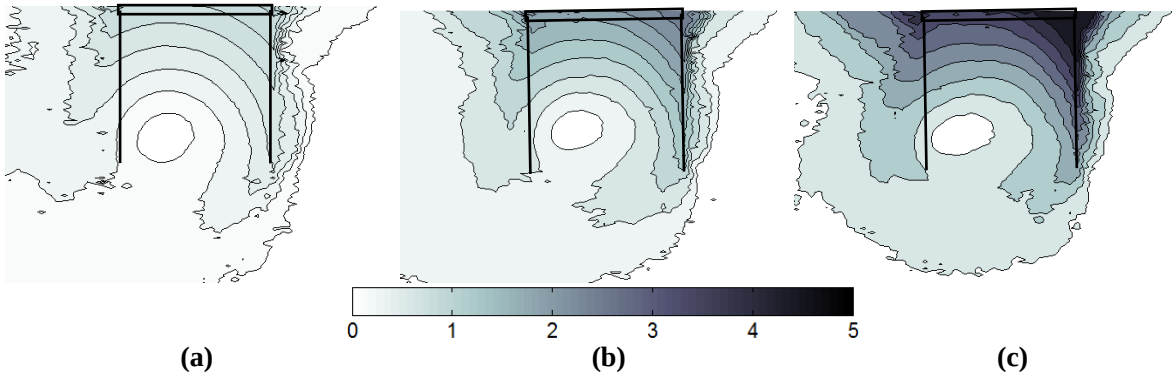

Figure 12. Particle displacement field when caisson rotational angle is 0.2º (a), 0.5º (b) and 1.0º (c)

The averaged micro-pure rotation rate (APR) field for the caisson rotational angle of 0.2º, 0.5º and 1.0º is shown in Figure 13. The APR is defined as

$$\text{APR}=\frac{1}{N}\sum_{k=1}^{N}\left[\frac{1}{r}\left(\dot{\theta}_1^k r_1+\dot{\theta}_2^k r_2\right)\right],\ r=\frac{2r_1r_2}{r_1+r_2} \quad \text{.....(1)}$$

where N is the number of contacts; $\dot{\theta}_1^k$ and $\dot{\theta}_2^k$ are the angular velocities of two contacting particles with radii r_1 and r_2. At the microscale, the APR is a transient variable relating to particle rotation (sliding) and particle size. At the macroscale, it is a non-linear function of the macro-rotation rate of the major principal axis of stress and contributes to the energy dissipation in granular materials (Jiang et al., 2005). In addition, APR is also closely related to the macroscopic deformation of granular materials (Wang and Arson 2018). Figure 13

shows the APR is large for soils inside the caisson, in the passive region and in the active region before the foundation failure, and becomes localized near the right wall of the foundation after failure.

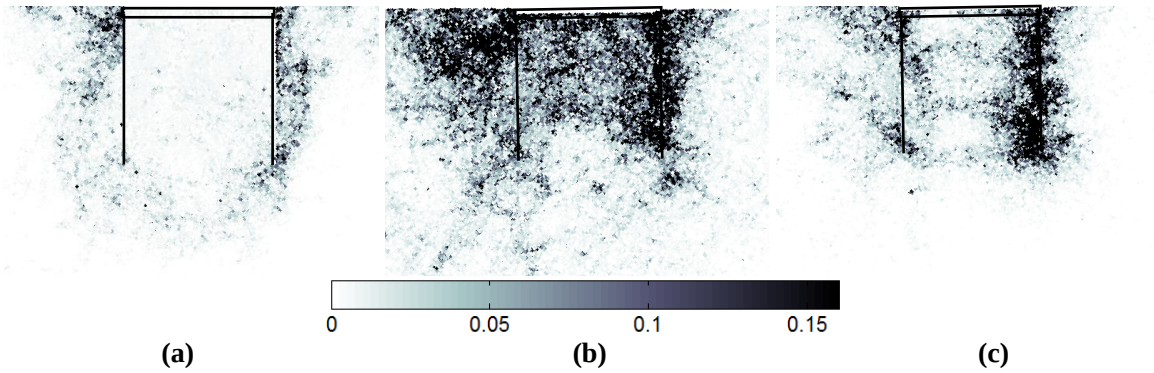

Figure 13. Averaged micro-pure rotation rate field when caisson rotational angle is 0.2° (a), 0.5° (b) and 1.0° (c)

Figure 14 shows the vertical stress distribution. Compared with the vertical stress distribution after the insertion process in Figure 10(b), the stress near the left skirt is increased while the stress on near the right skirt is decreased. When the caisson rotates anticlockwise, the soils near the left are compacted due the penetration of the skirt, which induces the stress increase. And soils at the tip of the left skirt have the largest stress increase. On the other hand, soils on the on the right side are unloaded due to the removal of the skirt.

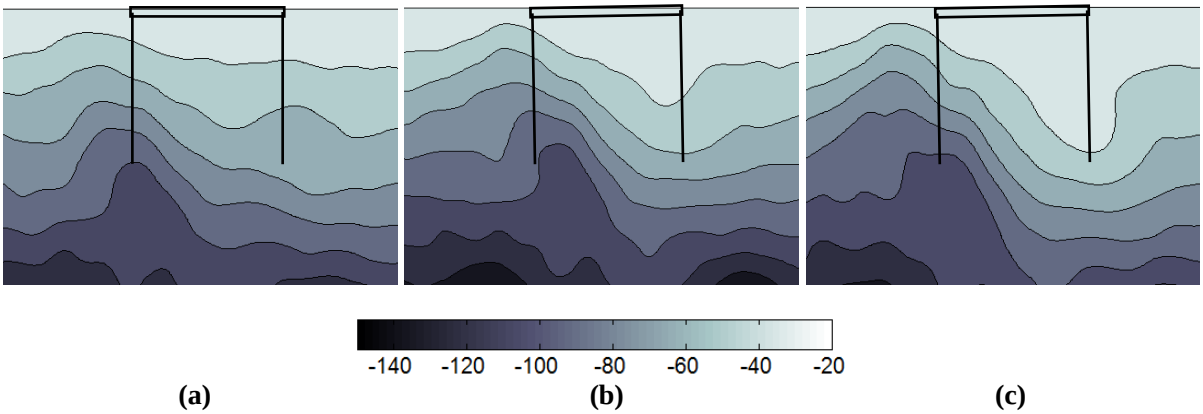

Figure 14. Vertical ground stress distribution when caisson rotational angle is 0.2° (a), 0.5° (b) and 1.0° (c)

The force chain distribution at different loading stages is shown in Figure 15. Because the caisson rotates counter clockwise, the magnitude and density of force chains near the upper left and the lower right of the caisson, which regions are marked by the two red squares with solid lines in Figure 15(c), keep increasing as the rotational angle increases. In addition, due to the internal "inverted" scoop mechanism developing within the soil plug (Barari and Ibsen 2012), contact forces between particles in the lower left part of the soil plug and the left skirt (red squares with dash lines in Figure 15(c)) are also increased.

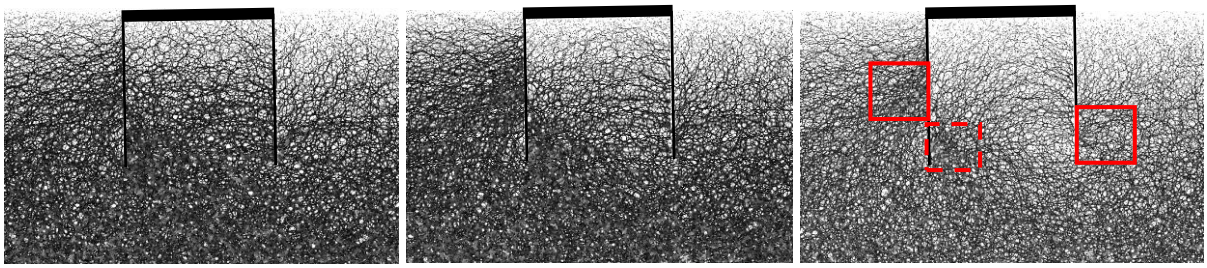

(a) **(b)** **(c)**

Figure 15. Force chain distribution when caisson rotational angle and maximum contact force are 0.2º and 2.5 kN (a), 0.5º and 2.6 kN (b) and 1.0º and 2.7 kN (c)

3.2.2. Evolution of particle fabric

The behavior of soils is known to be sensitive to the material fabric which is the topology of the internal structure of the soil particles. A lot of previous studies have been qualitatively related the soil fabric change to the macroscale observations of soil response (Chen et al., 2020; Fonseca et al., 2013; Gao and Zhao 2013; Jiang et al., 2019; Oda et al., 1982; Wang et al., 2019). Therefore, in order to better understand the failure mechanism of caisson foundation, the fabric evolution from the initial stage to the failure stage is investigated in this section.

According to the results in Section 3.2.1 and Figure 11 to 14, soils exhibit quite different behaviors depending on their relative positions with the caisson. For example, soil particles inside passive or active regions have much large rotation than soils in other areas according

to Figure 11. In order to better describe the fabric of soils, the soil particles are divided into four groups, i.e. LS, RS, IN, OUT, which corresponds to soil particles on the left side, on the right side, inside or outside of the caisson (Figure 16). The two triangular regions in Figure 16, which consist of the LS and RS groups, have the same size and shape with the passive region and active region in Figure 11. Caisson foundations are often subjected to large horizontal force and overturning moments. The bearing capacity of horizontal force is determined by the total passive earth pressure from the passive region LS and the horizontal friction at the bottom. Therefore, soils with large friction angle can stand higher horizontal force. In terms of the bearing capacity of moment, because the rotation center of the caisson foundation is located at the lower left part (Figure 12), soils at different regions contribution to the capacity with different mechanisms.

Three fabric descriptors are investigated in this study, i.e. particle contact orientation, normal contact force and shear contact force. For a contact between two spherical particles, the contact orientation is defined as the normalized vector connecting centroids of the two particles. Normal and shear contact forces are the force in parallel and vertical to the contact direction. For a granular assembly, the contact orientation distribution can be characterized by an angular distribution $E(\theta)$, which is given by

$$E(\theta) = \frac{1}{2\pi}[1 + a\cos 2(\theta - \theta_a)] \quad \text{.....(2)}$$

where a defines the magnitude of anisotropy and θ_a defines the direction of anisotropy (Rothenburg and Bathurst 1989). Similarly, the normal force distribution and shear force distribution can be expressed as

$$f_n(\theta) = f_{n0}[1 + a_n \cos 2(\theta - \theta_n)] \quad \text{.....(3)}$$

and

$$f_s(\theta) = -f_{s0} a_s \sin 2(\theta - \theta_s) \quad \text{.....(4)}$$

where f_{n0} / f_{s0} is the average normal/shear force over all contacts in the assembly, a_n / a_s defines normal/shear force anisotropy, and θ_n / θ_s is the principal direction of the normal/shear contact force.

The fabric evolution of particles in the LS group when the rotational angle is 0.0º, 0.2º, 0.5º and 1.0º is shown in Figure 17 in which the black lines represents the data measured in the DEM simulations and red lines are the analytical approximations based on Eq. (2) to (4). In Figure 17, good agreements can be observed between the measured results and the analytical approximations. Before applying moments and horizontal loads to the foundation, the contact orientation and normal contact force have an almost uniform angular distribution (Figure 17(a) and (b)), and the peak shear forces are in the vertical and horizontal direction (Figure 17(c)). These observations demonstrate that insertion process generated very slight anisotropy in the soils on the left side, which conforms with the results in Section 3.1. In the loading process, significant anisotropy can be observed in Figure 17(d) to (l). When the rotational angle is increased from 0.0º to 1.0º, the contact orientation anisotropy parameters a increases from 0.07 to 0.20 while the θ_a remains at 12º (Figure 17(a), (d), (g) and (j)). This evolution of contact orientation indicates that the magnitude of anisotropy keeps increasing but the direction remains same during the loading process. The increased contact anisotropy in the upper right to low left direction is induced by the combined horizontal movement and counterclockwise rotation of the caisson. Similar evolution pattern is obtained for the normal contact force distribution, which has the final a_n and θ_n equal to 0.55 and 20º, respectively. The evolution of contact orientation is consistent with force change in the LS region in Figure 15: the combined horizontal and counter clockwise rotational movement of the caisson generated new contacts and force chains in the moving direction. In addition, the magnitude

of contact force is also increased due to the passive movement of particles in the LS region. In terms of the shear contact force, the anisotropy magnitude a_s keeps increasing and the anisotropy direction θ_s decreases to resist the external shear force imposed by the caisson. Anisotropy is also generated in other areas, summarized in Table 2. The parameters a and a_n for soils in the LS and RS groups are much larger than soils in other places, which demonstrates the large anisotropy in these areas. To sum up, the movement of caisson, which is induced by the load combination imposed on the caisson, introduces anisotropy in the soils, and the magnitude and direction of the anisotropy are determined by their relative position to the caisson.

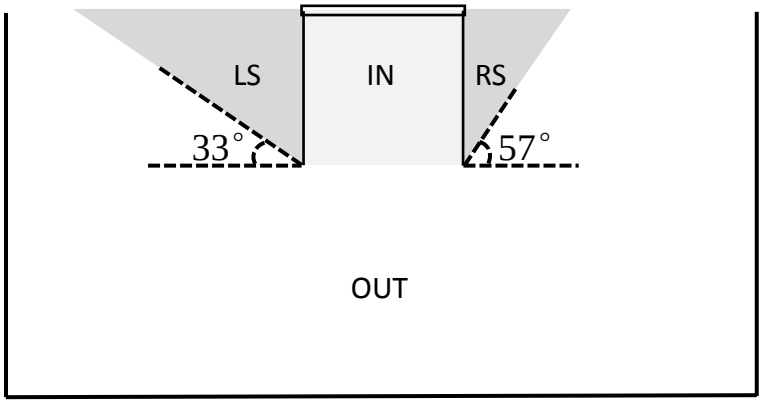

Figure 16. Schematic diagram of grouping method of soil particles

Rotational angle (°)	Contact orientation distribution	Normal contact force distribution	Shear contact force distribution
0.0	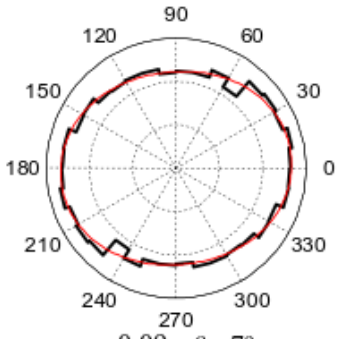 a=0.09, θ_a=7° (a)	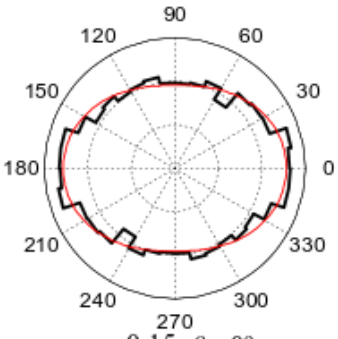 a_n=0.15, θ_n=0° (b)	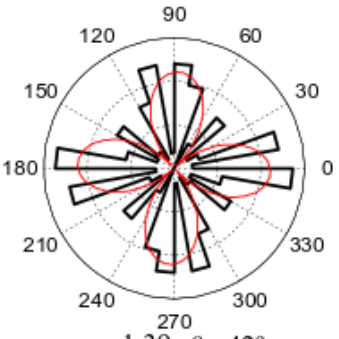 a_s=1.39, θ_s=42° (c)
0.2	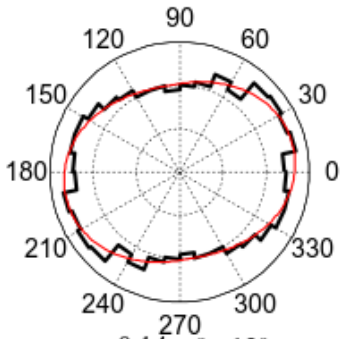 a=0.14, θ_a=12° (d)	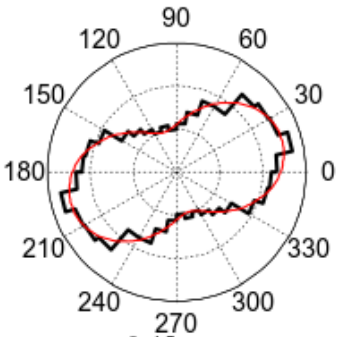 a_n=0.45, θ_n=17° (e)	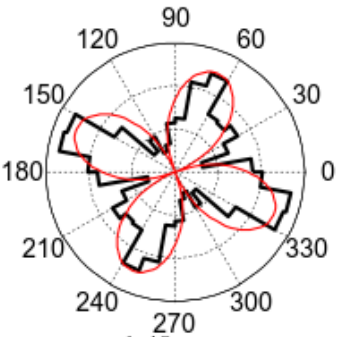 a_s=1.48, θ_s=22° (f)
0.5	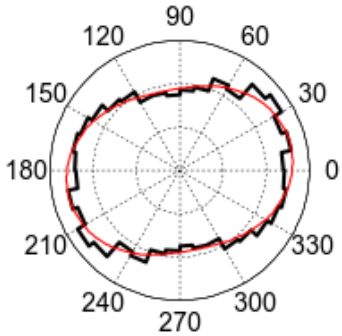 a=0.17, θ_a=12° (g)	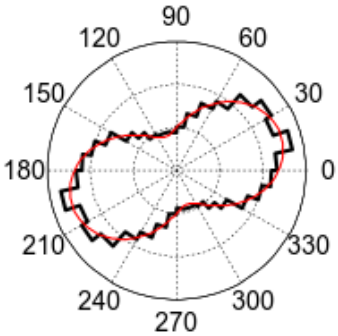 a_n=0.51, θ_n=19° (h)	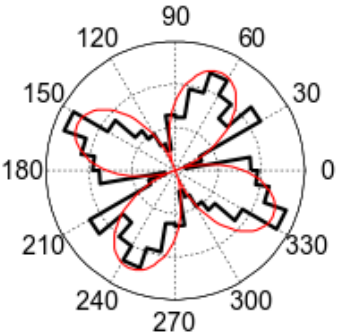 a_s=1.51, θ_s=19° (i)
1.0	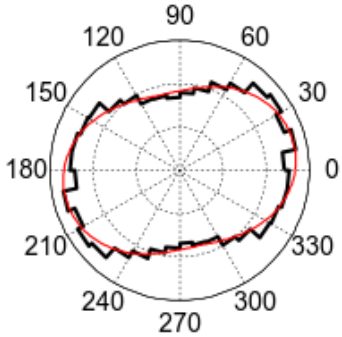 a=0.20, θ_a=12° (j)	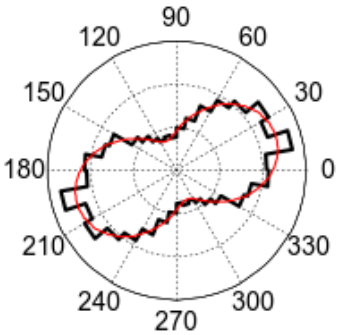 a_n=0.55, θ_n=20° (k)	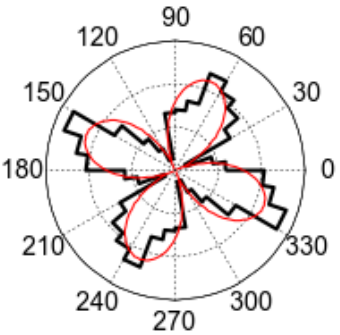 a_s=1.56, θ_s=23° (l)

Figure 17. Fabric evolution of particles in the LS group

Table 2. Summary of soil anisotropy induced by the foundation failure

Fabric descriptor		LS	RS	IN	OUT
Contact orientation	a (-)	0.20	0.14	0.08	0.02
	θ_a (°)	12	72	11	12
Normal contact force	a_n (-)	0.55	0.38	0.21	0.02
	θ_n (°)	20	59	19	75
Shear contact force	a_s (-)	1.56	1.36	1.50	1.38
	θ_s (°)	23	55	31	74

3.3. Effect of M/(DH)

When the suction caissons are used as foundations for offshore wind turbines, they are often subjected to high overturning moment. Two kinds of arrangements of caissons are often used as foundations for wind turbines, i.e. the tetrapod and the monopod. For the monopod condition, the key issue is the performance of foundations under high overturning moment. Therefore, the effect of the dimensionally homogeneous moment to horizontal load ratio, M/(DH), on the behavior of caisson foundations is investigated in this section. The following discussions are based on the results of tests 10g_1.1 and 10g_8.748. However, the conclusions are applicable to tests with various values of M/(DH).

Figure 18 shows the particle rotation of soils when the value of M/(DH) equals to 1.1 and 8.748. Similar with the results in the 1g_1.1 test in Figure 11(c), the passive failure zone and active failure zone on the left and right side of the caisson can be observed in both tests. For particles inside the caisson, large rotation occurs near the skirts. Particles in other areas experienced relatively smaller rotations. The comparison of the results between Figure 18(a) and (b) shows that the passive and active failure zones are smaller in the 10g_1.1 test. In other words, foundations with lower M/(DH) ratio has larger passive and active failure zones. The effect of M/(DH) on the size of failure zones can also be identified from the results of particle displacement shown in Figure 19, which clearly presents smaller sizes of two failure

zones in the 10g_1.847 test. The smaller failure zone sizes provide the explanation of the lower bearing capacities of horizontal load and overturning moment in Figure 5 and Figure 6. Figure 20 shows the APR field of the two tests. Except for a larger failure region in the 10g_1.1 test, an increased magnitude of APR can also be observed. The vertical ground stress distributions of the two tests are shown in Figure 21 in which similar distributions can be observed. Therefore, the M/(DH) ratio does not have a strong influence on the vertical stress distribution. Figure 22 presents the force chain distribution of the two tests, in which a strong similarity is found on the locations and magnitude of the localized strong force chains. Therefore, the effect of M/(DH) ratio on the force chain is very slight.

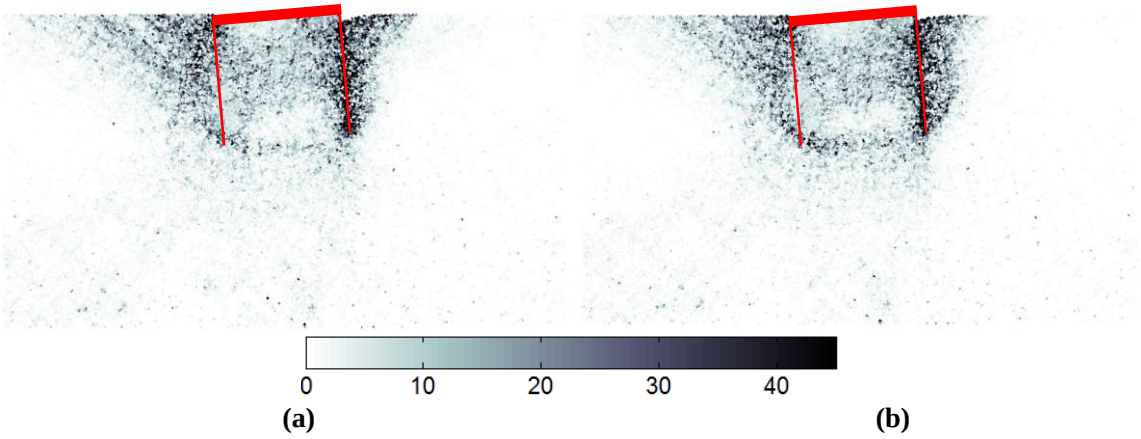

Figure 18. Particle rotation with M/(DH) equal to 1.1 (a) and 8.748 (b)

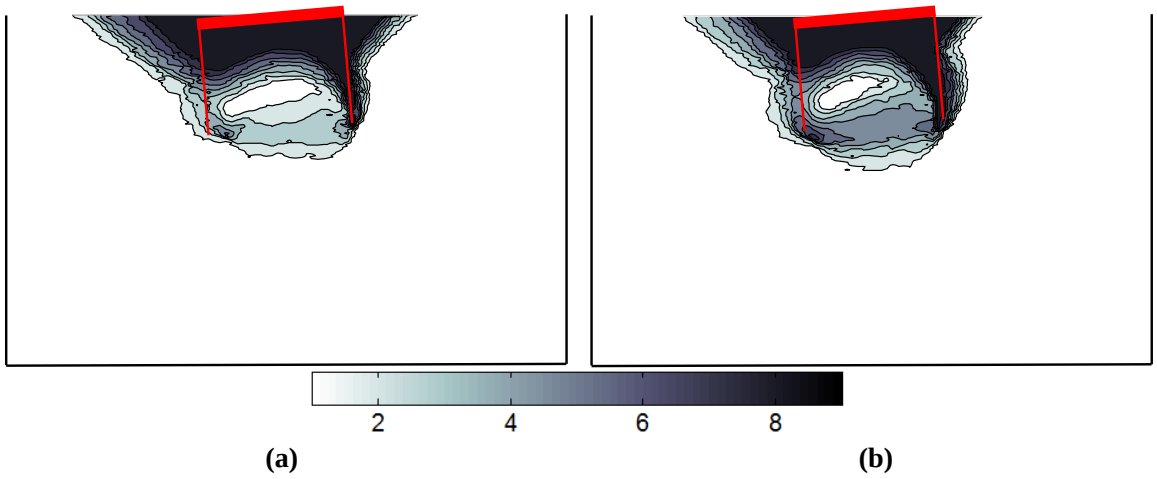

Figure 19. Particle displacement with M/(DH) equal to 1.1 (a) and 8.748 (b)

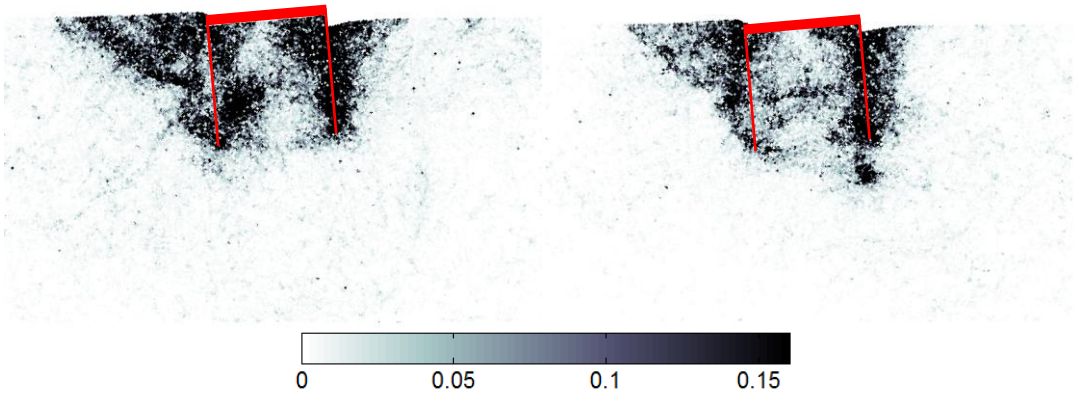

Figure 20. Averaged micro-pure rotation rate field with M/(DH) equal to 1.1 (a) and 8.748 (b)

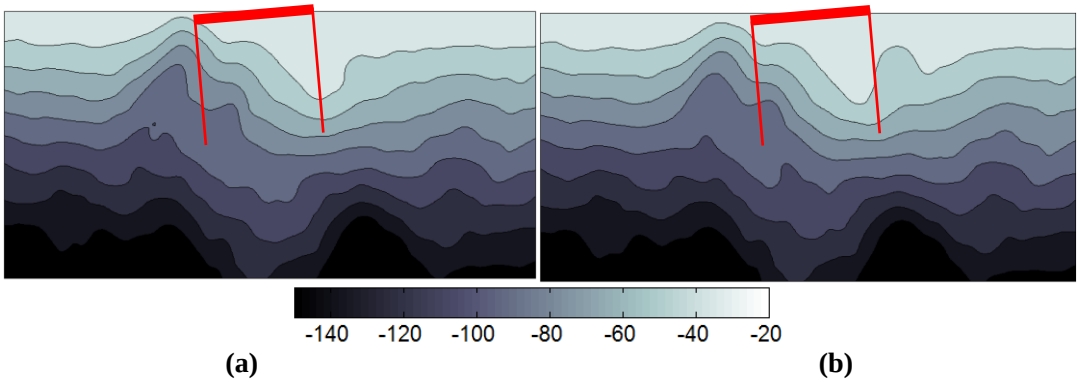

Figure 21. Vertical ground stress distribution with M/(DH) equal to 1.1 (a) and 8.748 (b)

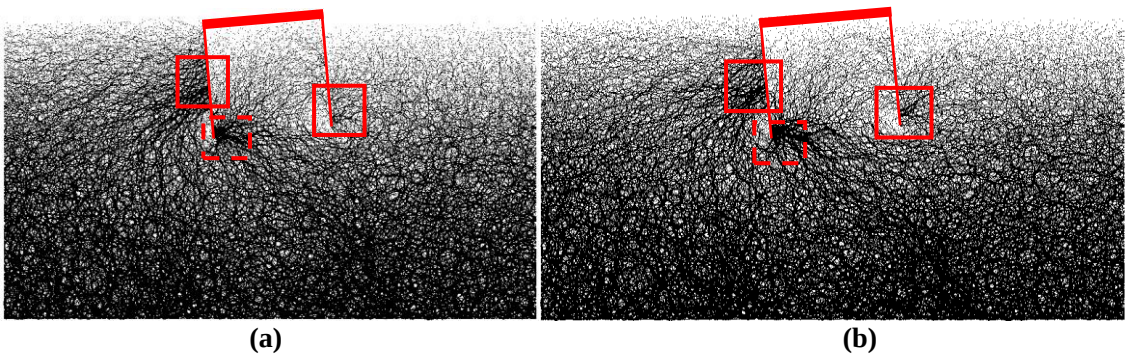

Figure 22. Force chain distribution with M/(DH) and maximum contact force equal to 1.1 and 2.70 kN (a), and 8.748 and 2.67 kN (b)

4. Conclusion

In this study, the DEM simulations of caisson foundation subjected to different load combinations have been conducted. Simulation results have the same pattern with the experimental results, which indicates the validity of the DEM model. Then the micro-mechanical analysis of the behaviors of a caisson foundation during its installation, operation and progressive failure have been conducted. In addition, the effect of dimensionally homogenous moment to horizontal load ratio (M/(DH)) is presented. The conclusions of this study includes:

(1) In the insertion process, the caisson foundation has a failure mechanism similar to the shallow foundation, in which a trapped triangle can be observed. Large particle rotation happens near the caisson and the boundaries of the trapped triangle below the caisson. In addition, particles inside the caisson and the trapped triangle also have large displacement.

(2) In the progressive failure process, the particle rotation and displacement increases with the rotational angle. The majority of particle sliding, which is characterized by the averaged micro-pure rotation rate (APR), occurs before the failure of the foundation. In addition, the increase of vertical stress in the passive region and the decrease of vertical stress in the active region are also observed.

(3) The particle fabric anisotropy mainly occurs within the active and passive regions. Soil particles are divided into four groups depending on their relative positons with the caisson. The rotational angle of the caisson induces significant fabric anisotropy which is characterized by contact orientation, normal contact force and shear contact force. Particles located in the passive region and active regions exhibits much large anisotropy magnitude compared with particles anywhere else.

(4) The homogenous moment to horizontal load ratio (M/(DH)) affects the size of the passive and active regions in the failure mechanism of caisson foundation: larger M/(DH) results in smaller passive and active regions.

This study is carried out to improve the understanding of the micro-mechanisms in the installation, operation and progressive failure processes of caisson foundation and provide helpful guidance on the design.

Acknowledgement

This research was financially supported by the Key Special Project for Introduced Talents Team of Southern Marine Science and Engineering Guangdong Laboratory (Guangzhou) (No.: GML2019ZD0503). The authors also would like to thank Mr. Honghao Lu who conducted a lot of numerical simulations for this study.

References

Achmus, M., Akdag, C.T., and Thieken, K., 2013. Load-bearing behavior of suction bucket foundations in sand. Applied Ocean Research, **43**: 157-165.

Bagheri, P., Son, S.W., and Kim, J.M., 2017. Investigation of the load-bearing capacity of suction caissons used for offshore wind turbines. Applied Ocean Research, **67**: 148-161.

Barari, A., and Ibsen, L.B., 2012. Undrained response of bucket foundations to moment loading. Applied Ocean Research, **36**: 12-21.

Cassidy, M.J., Randolph, M.F., and Byrne, B.W., 2006. A plasticity model describing caisson behaviour in clay. Applied Ocean Research, **28**(5): 345-358.

Ceccato, F., Beuth, L., Vermeer, P.A., and Simonini, P., 2016. Two-phase Material Point Method applied to the study of cone penetration. Computers and Geotechnics, **80**: 440-452.

Chai, J.C., Hossain, M.J., Carter, J., and Shen, S.L., 2014. Cone penetration-induced pore pressure distribution and dissipation. Computers and Geotechnics, **57**: 105-113.

Chen, W.-B., Liu, K., Yin, Z.-Y., and Yin, J.-H., 2020. Crushing and Flooding Effects on One-Dimensional Time-Dependent Behaviors of a Granular Soil. **20**(2): 04019156.

Cox, J.A., O'Loughlin, C.D., Cassidy, M., Bhattacharya, S., Gaudin, C., and Bienen, B., 2014. Centrifuge study on the cyclic performance of caissons in sand. International Journal of Physical Modelling in Geotechnics, **14**(4): 99-115.

Cundall, P.A., and Strack, O.D.L., 1979. A discrete numerical model for granular assemblies. Geotechnique, **29**(1): 47-65.

Fan, Q.L., Luan, M.T., and Yang, Q. Three dimensional nonlinear finite element analyses for horizontal bearing capacity of deeply-embedded large-diameter cylindrical structure on soft ground. *In* 2006. pp. 521-530.

Foglia, A., Gottardi, G., Govoni, L., and Ibsen, L.B., 2015. Modelling the drained response of bucket foundations for offshore wind turbines under general monotonic and cyclic loading. Applied Ocean Research, **52**: 80-91.

Fonseca, J., O'Sullivan, C., Coop, M.R., and Lee, P.D., 2013. Quantifying the evolution of soil fabric during shearing using directional parameters. Geotechnique, **63**(6): 487-499.

Fu, P.C., Walton, O.R., and Harvey, J.T., 2012. Polyarc discrete element for efficiently simulating arbitrarily shaped 2D particles. International Journal for Numerical Methods in Engineering, **89**(5): 599-617.

Gao, Z.W., and Zhao, J.D., 2013. Strain localization and fabric evolution in sand. International Journal of Solids and Structures, **50**(22-23): 3634-3648.

He, X., Wu, W., Cai, G., Qi, J., Kim, J.R., Zhang, D., and Jiang, M., 2020. Work–energy analysis of granular assemblies validates and calibrates a constitutive model. Granular Matter, **22**(1): 28.

He, X.Z., Liang, D.F., Wu, W., Cai, G.Q., Zhao, C.G., and Wang, S., 2018. Study of the interaction between dry granular flows and rigid barriers with an SPH model. International Journal for Numerical and Analytical Methods in Geomechanics, **42**(11): 1217-1234.

Jia, N., Zhang, P.Y., Liu, Y.G., and Ding, H.Y., 2018. Bearing capacity of composite bucket foundations for offshore wind turbines in silty sand. Ocean Engineering, **151**: 1-11.

Jiang, M.J., and Yin, Z.Y., 2012. Analysis of stress redistribution in soil and earth pressure on tunnel lining using the discrete element method. Tunnelling and Underground Space Technology, **32**: 251-259.

Jiang, M.J., and Yin, Z.Y., 2014. Influence of soil conditioning on ground deformation during longitudinal tunneling. Comptes Rendus Mecanique, **342**(3): 189-197.

Jiang, M.J., Konrad, J.M., and Leroueil, S., 2003. An efficient technique for generating homogeneous specimens for DEM studies. Computers and Geotechnics, **30**(7): 579-597.

Jiang, M.J., Harris, D., and Yu, H.S., 2005. Kinematic models for non-coaxial granular materials. Part I: theory. International Journal for Numerical and Analytical Methods in Geomechanics, **29**(7): 643-661.

Jiang, M.J., Yin, Z.Y., and Shen, Z.F., 2016. Shear band formation in lunar regolith by discrete element analyses. Granular Matter, **18**(2).

Jiang, M.J., Zhang, A., and Li, T., 2019. Distinct element analysis of the microstructure evolution in granular soils under cyclic loading. Granular Matter, **21**(2).

Jin, Z., Yin, Z.Y., Kotronis, P., and Li, Z., 2019a. Advanced numerical modelling of caisson foundations in sand to investigate the failure envelope in the H-M-V space. Ocean Engineering, **190**.

Jin, Z., Yin, Z.Y., Kotronis, P., and Jin, Y.F., 2019b. Numerical investigation on evolving failure of caisson foundation in sand using the combined Lagrangian-SPH method. Marine Georesources & Geotechnology, **37**(1): 23-35.

Jin, Z., Yin, Z.Y., Kotronis, P., Li, Z., and Tamagnini, C., 2019c. A hypoplastic macroelement model for a caisson foundation in sand under monotonic and cyclic loadings. Marine Structures, **66**: 16-26.

Kelly, R.B., Houlsby, G.T., and Byrne, B.W., 2006. A comparison of field and laboratory tests of caisson foundations in sand and clay. Geotechnique, **56**(9): 617-626.

Kou, H.L., Yang, D.L., Zhang, W.C., Wu, Y.F., and Fu, Q., 2019. Model tests on performance of offshore wind turbine with suction caisson foundation in sand. Marine Georesources & Geotechnology.

Lyu, H.-M., Shen, S.-L., Zhou, A., and Yang, J., 2019. Risk assessment of mega-city infrastructures related to land subsidence using improved trapezoidal FAHP. Science of The Total Environment: 135310.

Mehravar, M., Harireche, O., and Faramarzi, A., 2016. Evaluation of undrained failure envelopes of caisson foundations under combined loading. Applied Ocean Research, **59**: 129-137.

Mehravar, M., Harireche, O., Faramarzi, A., and Alani, A.M., 2017. Modelling the variation of suction pressure during caisson installation in sand using FLAC3D. Ships and Offshore Structures, **12**(7): 893-899.

Nguyen-Sy, L., and Houlsby, G.T., 2005. The theoretical modelling of a suction caisson foundation using hyperplasticity theory. Frontiers in Offshore Geotechnics II, Perth: 417.

Oda, M., Nematnasser, S., and Mehrabadi, M.M., 1982. A Statistical Study of Fabric in a Random Assembly of Spherical Granules. International Journal for Numerical and Analytical Methods in Geomechanics, **6**(1): 77-94.

Pradana, M.R., Qian, X.D., and Ahmed, A., 2019. Efficient discrete element simulation of managed ice actions on moored floating platforms. Ocean Engineering, **190**.

Rothenburg, L., and Bathurst, R.J., 1989. Analytical Study of Induced Anisotropy in Idealized Granular-Materials. Geotechnique, **39**(4): 601-614.

Schneider, J.A., and Senders, M., 2010. Foundation Design: A Comparison of Oil and Gas Platforms with Offshore Wind Turbines. Marine Technology Society Journal, **44**(1): 32-51.

Skau, K.S., Grimstad, G., Page, A.M., Eiksund, G.R., and Jostad, H.P., 2018. A macro-element for integrated time domain analyses representing bucket foundations for offshore wind turbines. Marine Structures, **59**: 158-178.

Takahashi, H., Sassa, S., Morikawa, Y., Takano, D., and Maruyama, K., 2014. Stability of caisson-type breakwater foundation under tsunami-induced seepage. Soils and Foundations, **54**(4): 789-805.

Tang, X.W., Zhang, X.W., Shao, Q., and Li, Z.Q., 2016. Rotation Center and Horizontal Bearing Capacity of the Bucket Foundation in Soft Ground. Marine Georesources & Geotechnology, **34**(6): 594-601.

Villalobos, F.A., Byrne, B.W., and Houlsby, G.T., 2009. An Experimental Study of the Drained Capacity of Suction Caisson Foundations under Monotonic Loading for Offshore Applications. Soils and Foundations, **49**(3): 477-488.

Wang, P., and Arson, C., 2018. Energy distribution during the quasi-static confined comminution of granular materials. Acta Geotechnica, **13**(5): 1075-1083.

Wang, P., Karatza, Z., and Arson, C., 2019. DEM modelling of sequential fragmentation of zeolite granules under oedometric compression based on XCT observations. Powder Technology, **347**: 66-75.

Wu, Y.-X., Shen, S.-L., Lyu, H.-M., and Zhou, A., 2020. Analyses of leakage effect of waterproof curtain during excavation dewatering. Journal of Hydrology, **583**: 124582.

Xiong, H., Nicot, F., and Yin, Z.Y., 2019a. From micro scale to boundary value problem: using a micromechanically based model. Acta Geotechnica, **14**(5): 1307-1323.

Xiong, H., Yin, Z.Y., and Nicot, F., 2019b. A multiscale work-analysis approach for geotechnical structures. International Journal for Numerical and Analytical Methods in Geomechanics, **43**(6): 1230-1250.

Yun, G., and Bransby, M.F., 2007. The undrained vertical bearing capacity of skirted foundations. Soils and Foundations, **47**(3): 493-505.

Zhao, C.-F., Yin, Z.-Y., Misra, A., and Hicher, P.-Y., 2018a. Thermomechanical formulation for micromechanical elasto-plasticity in granular materials. International Journal of Solids and Structures, **138**(1): 64-75.

Zhao, C.-F., Yin, Z.-Y., and Hicher, P.-Y., 2018b. Integrating a micromechanical model for multiscale analyses. International Journal for Numerical Methods in Engineering, **114**(2): 105-127.

Zhao, C.-F., Yin, Z.-Y., and Hicher, P.-Y., 2018c. A multiscale approach for investigating the effect of microstructural instability on global failure in granular materials. International Journal for Numerical and Analytical Methods in Geomechanics, **42**(17): 2065-2094.

Zhu, B., Kong, D.Q., Chen, R.P., Kong, L.G., and Chen, Y.M., 2011. Installation and lateral loading tests of suction caissons in silt. Canadian Geotechnical Journal, **48**(7): 1070-1084.

Zhu, F.Y., Bienen, B., O'Loughlin, C., Cassidy, M.J., and Morgan, N., 2019a. Suction caisson foundations for offshore wind energy: cyclic response in sand and sand over clay. Geotechnique, **69**(10): 924-931.

Zhu, H.X., and Yin, Z.Y., 2019. Grain Rotation-Based Analysis Method for Shear Band. Journal of Engineering Mechanics, **145**(10).

Zhu, H.X., Zhou, W.H., and Yin, Z.Y., 2018. Deformation mechanism of strain localization in 2D numerical interface tests. Acta Geotechnica, **13**(3): 557-573.

Zhu, H.X., Yin, Z.Y., and Zhang, Q., 2019b. A novel coupled FDM-DEM modelling method for flexible membrane boundary in laboratory tests. International Journal for Numerical and Analytical Methods in Geomechanics.

Figure captions

Figure 19. Particle displacement with M/(DH) equal to 1.1 (a) and 8.748 (b)

Figure 20. Averaged micro-pure rotation rate field with M/(DH) equal to 1.1 (a) and 8.748 (b)

Figure 21. Vertical ground stress distribution with M/(DH) equal to 1.1 (a) and 8.748 (b)

Figure 22. Force chain distribution with M/(DH) and maximum contact force equal to 1.1 and 2.70 kN (a), and 8.748 and 2.67 kN (b)